Rare Metal Materials and Engineering
Volume 52, Issue 1, January 2023
Available online at www.rmme.ac.cn

Science Press

Cite this article as: Xia Yuanjia, Zhao Fang, Li Zhizun, et al. Laser Absorption and Infrared Emissivity of $Sn_{1-x}Sm_xO_2$ Micro/Nano-Fibers: Experimental Study and First-Principles Simulation[J]. Rare Metal Materials and Engineering, 2023, 52(01): 31-40.

ARTICLE

Laser Absorption and Infrared Emissivity of $Sn_{1-x}Sm_xO_2$ Micro/Nano-Fibers: Experimental Study and First-Principles Simulation

Xia Yuanjia[1], Zhao Fang[1], Li Zhizun[1], Cheng Zhaogang[1], Xu Baocai[2]

[1] Shijiazhuang Campus, Army Engineering University of PLA, Shijiazhuang 050003, China; [2] Hebei Vocational University of Industry and Technology, Shijiazhuang 050091, China

Abstract: $Sn_{1-x}Sm_xO_2$ (x=0wt%, 8wt%, 16wt%, 24wt%) micro/nano-fibers were prepared by electrospinning combined with heat treatment. The phase, morphology, infrared emissivity, and laser absorption properties of the products were characterized. The first principles simulation based on density functional theory was used to compare and analyze the photoelectric properties of $Sn_{1-x}Sm_xO_2$ (x=0wt%, 16wt%) material, and the effect mechanism of Sm^{3+} doping on the infrared emissivity and laser absorption of SnO_2 from the perspective of electronic structure was further clarified. Results show that after calcination at 600 °C, the calcined $Sn_{1-x}Sm_xO_2$ micro/nano-fibers all present the single rutile structure and show good fiber morphology. The fibers interlace with each other, forming irregular three-dimensional network structure, and the elements are evenly distributed on the fiber. With increasing the Sm^{3+} doping amount, the reflectivity of $Sn_{1-x}Sm_xO_2$ micro/nano-fibers is decreased gradually at wavelength of 1.06 and 1.55 μm, and the infrared emission is decreased firstly and then increased. When x=16wt%, the reflectivity at wavelength of 1064 nm is 53.9%, the reflectivity at wavelength of 1550 nm is 38.5%, and the infrared emissivity at wave band of 8–14 μm is 0.749, which provides a theoretical and practical basis for the thin, light, wide-band, and high-performance laser-infrared compatible stealth materials.

Key words: micro/nano-fibers; laser absorption; infrared emissivity; first principles; semiconductor

With the continuous development of military technology and the advent of various advanced detectors, the traditional single-function camouflage coating faces severe challenges. The multi-spectra compatible stealth materials are required, and the development of effective laser-infrared compatible stealth material has been widely researched[1–2]. Laser-infrared compatible stealth materials have high reflection and low emission within the infrared bands (3–5 and 8–14 μm), and have low reflection and high absorption at the laser wavelengths of 1.06, 1.55, and 10.6 μm. Currently, the common laser and infrared compatible stealth materials mainly include the photonic crystals[3–4], metamaterials[5–6], and doped oxide semiconductors[7]. Photonic crystals and metamaterials are difficult to prepare, and the traditional composite coating of stealth materials is thick and dense[8], which is adverse to application. Therefore, it is of great significance to develop a thin compatible stealth material with easy preparation.

Oxide semiconductor materials have a broad application prospect in the infrared and laser compatible stealth fields[9]. It is found that the carrier concentration and plasma wavelength of oxide semiconductors can be adjusted by doping additives[10]. On the one hand, the strong absorption and excited radiation can be generated near the wavelength of 1.06 μm, and the laser absorption properties of oxide semiconductors can be improved. On the other hand, the resistivity and infrared emissivity of the doped system can be reduced for infrared stealth[9,11–12]. SnO_2, as a typical wide-gap N-type oxide semiconductor material, has stable physical and chemical properties, high visible light transmittance, and low resistivity, showing great potential as a photoelectric material[13–14]. Su et al[15] prepared $Sn_{1-x}Fe_xO_2$ (x=0, 0.03, 0.06,

Received date: April 15, 2022
Foundation item: Key Research and Development Program of Hebei Province (21351501D); Military Scientific Research Project (LJ20212C031165); Basic Frontier Science and Technology Innovation Project of Army Engineering University of PLA (KYSZJQZL2210)
Corresponding author: Zhao Fang, Master, Associate Professor, Shijiazhuang Campus, Army Engineering University of PLA, Shijiazhuang 050003, P. R. China, E-mail: zhaofang19821106@163.com

0.09) solid solution powder by coprecipitation method, and found that its infrared emissivity is decreased with increasing the Fe doping amount. Lu et al[16] doped SnO_2 with transition element oxides (Ni_2O_3/CuO/Sb_2O_3) and found that the prepared coating has good laser absorption performance. Rare earth elements can effectively improve the laser absorption performance of materials. Particularly, the transition from $^6H_{5/2}$ ground state into the $^6H_{9/2}$ excited state of Sm^{3+} ions leads to the strong absorption peak of 1050−1150 nm generated by the Sm-containing compounds, resulting in excellent laser absorption properties[17–19]. Zhang et al[20] prepared $SmB_{0.3}Al_{0.7}O_3$ powder by citric acid sol-gel combustion method, and found that absorption peaks appear at wavelength of 1.06 μm. $SmB_{0.3}Al_{0.7}O_3$ has the lowest reflectivity of 43.36% at wavelength of 1.06 μm. Li et al[21] prepared $SmCrO_3$ powder material through the high-temperature solid-phase method. At the calcination temperature of 1400 °C, the specimen with thickness of 0.2 mm shows strong absorption peaks at wavelength of 1.06 and 1.55 μm, and the corresponding absorption ratios are 54% and 53%, respectively, showing good laser stealth performance. Micro/nano-fiber materials have large specific surface area, light-weight, and high porosity[22], presenting great potential in the stealth material field[1,23]. However, the infrared and laser compatible stealth properties of fibrous rare earth element-modified tin oxide materials are rarely reported.

Therefore, in this research, $Sn_{1-x}Sm_xO_2$ (x=0wt%, 8wt%, 16wt%, 24wt%) micro/nano-fibers were prepared by electrostatic spinning process combined with heat treatment. The microstructure, laser absorption performance, and infrared emissivity of Sm^{3+}-doped SnO_2 were analyzed. Meanwhile, the doping model was established by the first-principles calculation, and the effect mechanism of Sm^{3+} doping on the laser absorption performance and infrared emissivity of SnO_2 materials was investigated from the perspective of electronic structure, providing a theoretical and practical basis for the further research of laser and infrared compatible stealth materials.

1 Experiment

$Zn_{1-x}Ce_xO$ (x=0, 0.02, 0.04, 0.06, 0.08) nano-fibers were prepared by the electrospinning method[24], and their microwave absorption properties and infrared emissivity were studied. When x=0.04, the minimum infrared emissivity of the specimen is 0.78. Meanwhile, $La_{1-x}Ba_xMnO_3$ ($0 \leqslant x \leqslant 0.5$) with perovskite structure was also prepared by the sol-gel method[25]. It is found that with increasing the Ba doping content, the infrared emissivity is firstly decreased and then increased. When x=0.3, the infrared emissivity is the lowest. Based on Ref. [25], the Sm doping content was set as 0wt%, 8wt%, 16wt%, and 24wt% in this research.

$SnCl_2 \cdot 2H_2O$ and $Sm(NO_3)_3 \cdot 6H_2O$ raw materials were dissolved in deionized water to prepare the product with stoichiometric ratio of $Sn_{1-x}Sm_xO_2$ (x=0wt%, 8wt%, 16wt%, 24wt%). Polyvinylpyrrolidone (PVP) and N/N-dimethylformamide (DMF) with the same mass were also dissolved in the water. Then the two solutions were mixed and stirred for 12 h to prepare the spinning precursor. The spinning precursor was transferred into a syringe with a stainless-steel needle (23G) for electrostatic spinning. The spinning process was conducted at room temperature with 20 kV in voltage, 20 cm in distance between the needle and the receiver, 0.1 mm/min in the solution propulsion rate, and 140 r/min in the receiving speed. The precursor micro/nano-fibers were dried at 100 °C for 12 h, then placed in an intelligent temperature control box resistance furnace, heated to 600 °C at heating rate of 1 °C/min, calcined for 2 h, and finally cooled to room temperature in furnace. The preparation process is shown in Fig.1.

Thermogravimetric analysis (TGA) and differential scanning calorimetry (DSC) were performed by SDT-Q600 thermal analyzer (TA Company). The phase of the specimens was analyzed by XD6 polycrystalline X-ray diffractometer (XRD). The model 380 Fourier Transform infrared spectrometer (FT-IR, Nicolet) was used to analyze the infrared spectra of specimens. SU-8010 field emission scanning electron microscope (SEM, Hitachi) was used to observe the specimen microstructures. The element composition of the product was analyzed by energy dispersive spectrometer (EDS, Genesis Apex2, USA). The full spectra and valence band spectra of the product were analyzed by X-ray photoelectron spectrometer (XPS, Thermo Scientific, K-Alpha, USA). Diffusion reflectivity of the product was tested by UV-3600 spectrophotometer and ISR-603 integrating sphere. The calcined products were mixed with epoxy resin with volume ratio of 1∶1, then coated on the high emissivity cera-mic sheets (diameter of 50 mm, thickness of 1 mm) with smooth surface by screen printing method, and finally dried at 100 °C for 2 h. After cooling to room temperature, ST2258C digital four-probe tester and IR-2 infrared emissivity tester were used to test the resistivity and infrared emissivity within the infrared bands (3 – 5 and 8 – 14 μm). UTi120S infrared thermal imager was used to capture the infrared thermal imaging images.

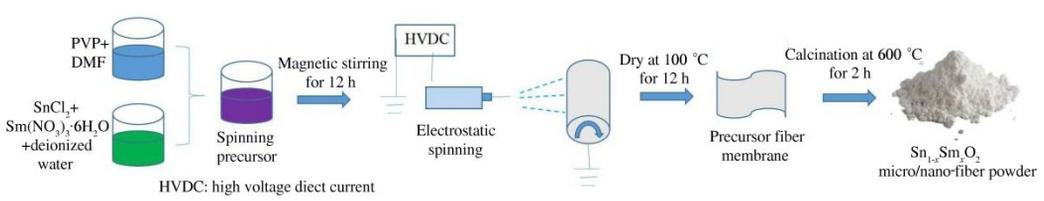

Fig.1 Schematic diagram of preparation process of $Sn_{1-x}Sm_xO_2$ micro/nano-fibers

CASTEP module in the Material Studio software was selected, the exchange-correlation function GGA, and the modified function PBE were used for calculation. The supersoft pseudopotential was used to approximately describe the interaction between valence electrons and ions. The parameters were as follows: the plane wave cutoff energy was 489.8 eV; the K-grid point of the Brillouin zone was 3×3×1; the unit electron energy was 2×10^{-5} eV/atom; the self-consistent accuracy was 2.0×10^{-6} eV/atom; the interatomic interaction force is less than 0.5 eV/nm; the stress deviation was less than 0.1 GPa. The selected valence electron configurations were Sn ($5s^25p^2$), O ($2s^22p^4$), and Sm ($5p^64f^66s^2$).

2 Results and Discussion

2.1 TGA-DSC analysis

Fig.2 shows the TGA-DSC curves of precursor $Sn_{1-x}Sm_xO_2$ fibers. According to Fig.2, the thermal decomposition process of precursor $Sn_{1-x}Sm_xO_2$ fibers can be divided into four stages. The first stage is from room temperature to 150 °C. The mass loss is about 9.5%, which is caused by the volatilization of residual solvent, the free water adsorbed on the precursor fiber surface, and the crystallization water in the raw material. The second stage is at 150–350 °C, and the mass loss is about 15.7%. According to the DSC curve, the small exothermic peak at 320 °C is mainly caused by the carbonization decomposition of the PVP side chain. The third stage is at 350–500 °C, showing a large mass loss of 39.6%. Meanwhile, the exothermic peak appears near 430 °C in the DSC curve, which is mainly due to the complete decomposition of PVP main chain and the gradual replacement of chlorine element by oxygen element. Therefore, $SnCl_2$ is gradually transformed into SnO_2. The fourth stage is over 500 °C. The mass barely changes and no exothermic peak appears in DSC curve, indicating that the thermal decomposition of the polymer in precursor fiber is completed, and $SnCl_2$ is completely transformed into SnO_2. Therefore, in order to fully crystallize the product, the calcination temperature of precursor $Sn_{1-x}Sm_xO_2$ fibers is set at 600 °C in this research.

2.2 XRD analysis

Fig.3 shows XRD patterns of $Sn_{1-x}Sm_xO_2$ (x=0wt%, 8wt%, 16wt%, 24wt%, 32wt%) micro/nano-fibers after calcination at 600 °C. As shown in Fig. 3, after calcination at 600 °C, obvious and sharp diffraction peaks of (110), (101), (200), (211), (220), (301), and (310) crystal planes can be observed in all specimens, and the intensities of the main diffraction peaks are arranged from strong to weak as (110)>(101)>(211)>(200). This result is consistent with JCPDF41-1445 reference, indicating that the products are all composed of single tetragonal rutile SnO_2. No characteristic diffraction peak of Sm^{3+} oxide can be observed in the calcined products, indicating that Sm^{3+} enters the lattice of SnO_2. Since the radius of Sm (0.16 nm) is close to that of Sn atom (0.18 nm), Sm atoms may enter the SnO_2 lattice by replacing Sn atoms. It is worth noting that when the Sm doping content is 32wt%, the crystallinity of SnO_2 is low and the original crystal structure of SnO_2 may be destroyed. Therefore, the maximum doping content is set as 24wt%.

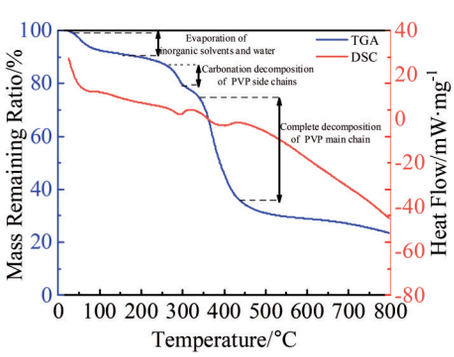

Fig.2 TGA-DSC curves of precursor $Sn_{1-x}Sm_xO_2$ micro/nano-fibers

2.3 FT-IR analysis

Fig.4 shows FT-IR spectra of $Sn_{1-x}Sm_xO_2$ micro/nano-fibers after calcination at 600 °C. It can be seen that all products have absorption peaks at 3435, 2361, 1642, and 618 cm^{-1}. The absorption peaks near 3435 and 1642 cm^{-1} are caused by the stretching vibration of O-H bond and the deformation vibration of adsorbed water, resulting from the adsorption of water vapor in the air by the product[26]. The absorption peak at 2361 cm^{-1} indicates CO_2, which can be attributed to the stretching vibration of CO_2 adsorbed onto the product[27]. The absorption peak near 618 cm^{-1} is the characteristic absorption peak of SnO_2 crystal, which can be attributed to the vibration band of Sn-O bond[28–29] with the E_uTO vibration mode[30]. Other special absorption peaks cannot be observed, which further indicates that the products after calcination at 600 °C are composed of single tetragonal rutile SnO_2.

2.4 SEM & EDS analysis

Fig. 5a and 5b show SEM morphologies of precursor $Sn_{1-x}Sm_xO_2$ micro/nano-fibers. It can be seen that the precursor

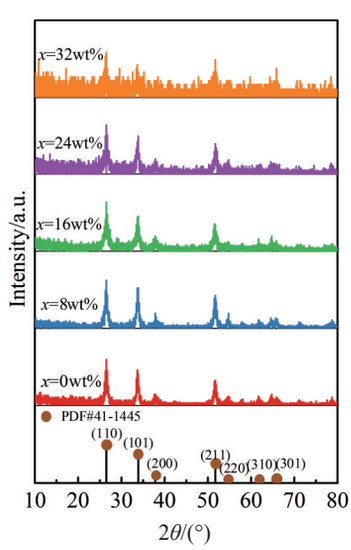

Fig.3 XRD patterns of $Sn_{1-x}Sm_xO_2$ micro/nano-fibers after calcination at 600 °C

fibers are continuous and uniformly distributed, forming an irregular network. According to Fig. 5b, the fiber surface is smooth and shows a network structure. The fiber diameter is 500 – 900 nm. Fig. 5c – 5f show SEM morphologies of $Sn_{1-x}Sm_xO_2$ micro/nano-fibers after calcination at 600 °C. The calcined products still maintain the fiber morphology, and their diameter is smaller than that of the precursor fiber, which is caused by the PVP decomposition during high-temperature calcination. Compared with that of the precursor fiber, the surface of $Sn_{1-x}Sm_xO_2$ micro/nano-fibers is slightly rough, which is composed of a large number of $Sn_{1-x}Sm_xO_2$ fine grains.

Fig. 6 shows EDS analysis results of $Sn_{0.84}Sm_{0.16}O_2$ micro/nano-fibers corresponding to Fig.5e. According to Fig.6a, only Sm, Sn, and O exist in the product, indicating that during the heat treatment process, PVP and other substances are completely decomposed. This result is consistent with XRD, FT-IR, TGA-DSC analysis results. According to Fig.6b–6e, all elements are evenly distributed in the fiber. The atomic ratio of Sm to Sn+Sm is about 16%, indicating that the $Sn_{0.84}Sm_{0.16}O_2$ micro/nanofibers have high purity and no impurities are prepared during the electrospinning process.

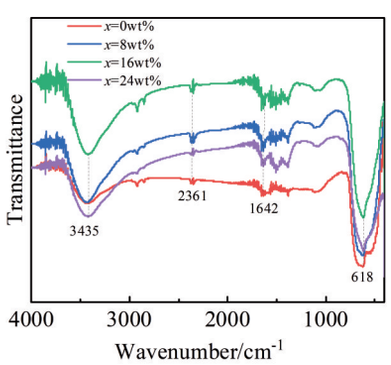

Fig.4 FT-IR spectra of $Sn_{1-x}Sm_xO_2$ micro/nano fibers after calcination at 600 °C

2.5 XPS analysis

Fig. 7 shows overall, Sn 3d, Sn 3d, and O 1s spectra of $Sn_{0.76}Sm_{0.24}O_2$ micro/nano-fibers. According to Fig. 7a, the binding energy peaks of C, O, Sn, and Sm can be observed. The C peak is caused by the carbon injection correction during the detection, and other substances cannot be detected. According to Fig.7b, the binding energy peaks near 486.4 (Sn $3d_{5/2}$) and 494.8 (Sn $3d_{3/2}$) eV correspond to Sn^{4+} [30], indicating that $SnCl_2$ is completely transformed into SnO_2 during the calcination. As shown in Fig.7c, the binding energy peaks near 1083 (Sm $3d_{5/2}$) and 1109.9 (Sm $3d_{3/2}$) eV correspond to Sm^{3+} [31], indicating that the Sm exists as Sm^{3+} in the fibers. As shown in Fig.7d, the binding energy peaks near 530.1, 531.0, and 533.3 eV correspond to lattice oxygen (O_{latt}), surface adsorbed oxygen (O_{ads}), and surface adsorbed water molecule (O_{H2O}), respectively[32]. These results all indicate that the pure $Sn_{1-x}Sm_xO_2$ fibers can be prepared by electrostatic spinning method.

2.6 Reflection performance

The reflectivity of $Sn_{1-x}Sm_xO_2$ micro/nano-fibers after calcination at wavelength of 500–2000 nm is shown in Fig.8a, and it can be divided into two parts: 500–1700 nm and 1700–2000 nm. When the wavelength is 500 – 1700 nm, the reflectivity of $Sn_{1-x}Sm_xO_2$ fibers is gradually decreased with increasing the Sm^{3+} doping amount. It can be seen that the $Sn_{0.84}Sm_{0.16}O_2$ and $Sn_{0.76}Sm_{0.24}O_2$ fibers have obvious absorption

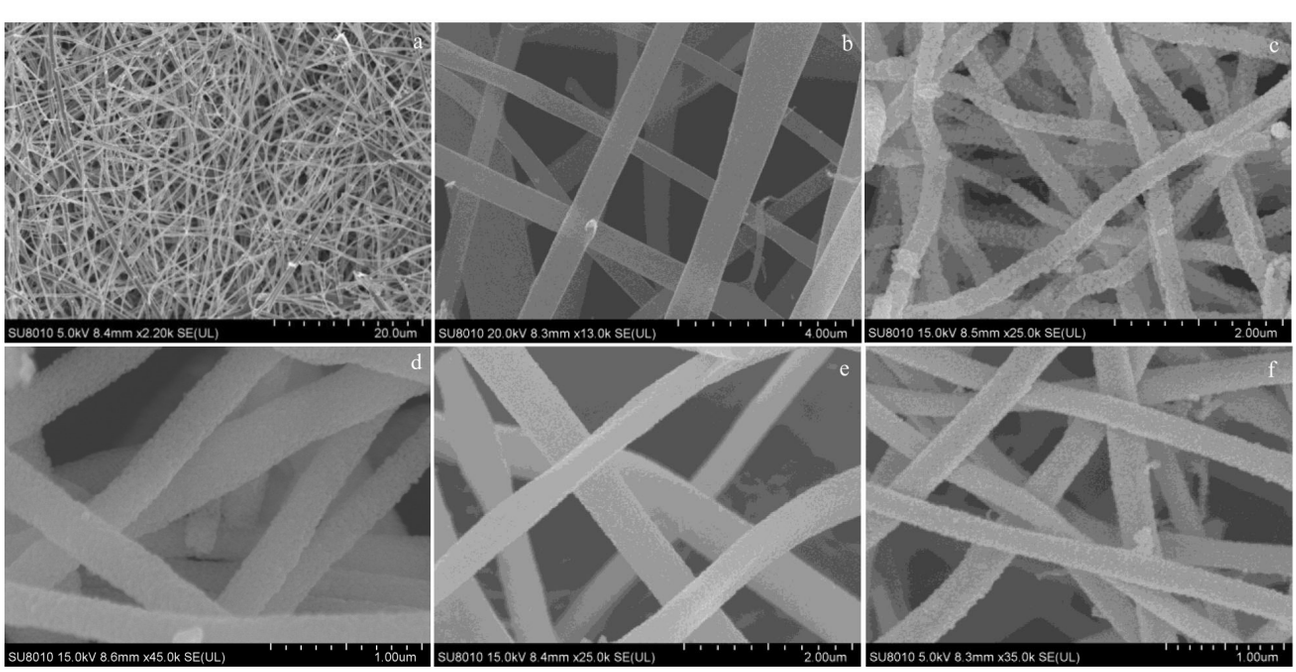

Fig.5 SEM morphologies of $Sn_{1-x}Sm_xO_2$ mico/nano-fibers before (a, b) and after (c–f) calcination at 600 °C: (c) x=0wt%, (d) x=8wt%, (e) x=16wt%, and (f) x=24wt%

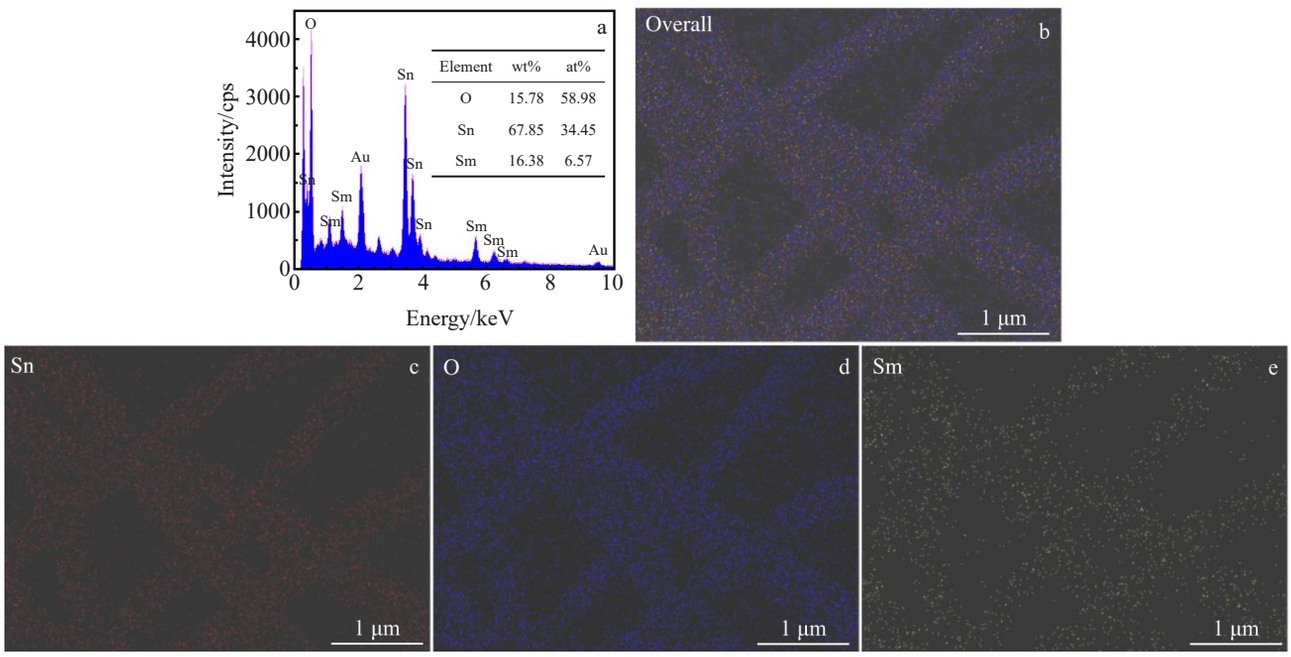

Fig.6 EDS analysis results (a) and element distributions (b–f) of $Sn_{0.84}Sm_{0.16}O_2$ micro/nano-fibers corresponding to Fig.5e: (b) overall, (c) Sn, (d) O, and (e) Sm

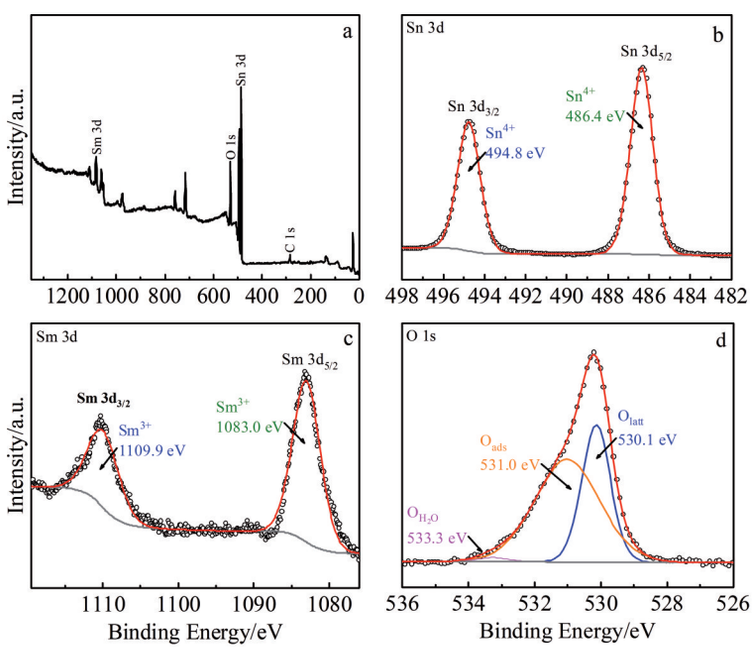

Fig.7 XPS spectra of $Sn_{0.76}Sm_{0.24}O_2$ micro/nano-fibers: (a) overall, (b) Sn 3d, (c) Sm 3d, and (d) O 1s

peaks at wavelength of 1000–1100 nm, which is favorable for the low reflectance at wavelength of 1064 nm. The reflectivity of $Sn_{0.84}Sm_{0.16}O_2$ and $Sn_{0.76}Sm_{0.24}O_2$ fibers at wavelength of 1064 nm is 53.9% and 50.5%, respectively. In addition, the wavelength of 1550 nm is a common working band of lasers, and the reflectivity of $Sn_{0.84}Sm_{0.16}O_2$ and $Sn_{0.76}Sm_{0.24}O_2$ fibers at this wavelength is 38.5% and 29.8%, respectively. When the wavelength is 1700–2000 nm, the reflectivity of $Sn_{0.76}Sm_{0.24}O_2$ fibers is low, while that of $Sn_{0.84}Sm_{0.16}O_2$ fibers is greater than that of SnO_2 and $Sn_{0.92}Sm_{0.08}O_2$ fibers. Thus, the higher reflectivity and lower emissivity in the infrared band can be achieved for the $Sn_{0.84}Sm_{0.16}O_2$ fibers. According to the semiconductor continuous spectrum theory, the propagation characteristics of light wave in the visible infrared band in the semiconductor are closely related to its plasma wavelength[33], which can be expressed by Eq.(1), as follows:

$$\lambda_p = 2\pi c\sqrt{\frac{m\varepsilon_0}{Ne^2}} \quad (1)$$

where λ_p is the plasma wavelength, m is the effective mass of the electron, ε_0 is the dielectric constant of the vacuum, N is

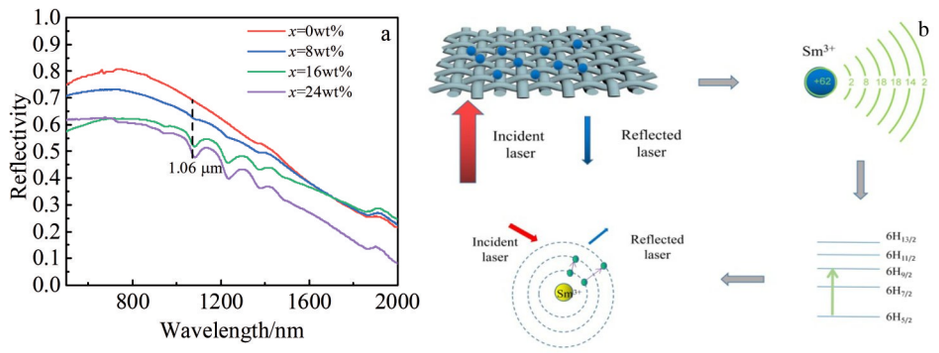

Fig.8 Reflectivity (a) and schematic diagram of reflection mechanism (b) of $Sn_{1-x}Sm_xO_2$ micro/nano-fibers

the carrier concentration, e is the electron charge, and c is the vacuum speed of light. When the wavelength of the incident light $\lambda > \lambda_p$, the semiconductor gradually exhibits the characteristics of metal and has a high reflectivity. This is because after Sm^{3+} doping, a new donor energy level is provided, free electrons are excited, and the carrier concentration is increased. The plasma wavelength of the system decreases, resulting in the better reflectivity of $Sn_{0.84}Sm_{0.16}O_2$ and $Sn_{0.92}Sm_{0.08}O_2$ fibers in 1700–2000 nm band, compared with that of the SnO_2[34–35]. However, excessive doping leads to the impurities and defects in the fibers. The scattered impurity ions change the mobility of carriers, reduce the concentration of carriers, and increase the plasma wavelength. Thus, the low reflectivity of $Sn_{0.76}Sm_{0.24}O_2$ fibers remains[35]. After doping Sm^{3+}, there are three reasons for the decrease in laser reflectivity for the doped fibers. Firstly, the micro/nano-fibers have large specific surface area and nonlinear characteristics, which promotes the charge transfer in the doped fibers and enables the light absorption performance of charges[22,36]. Secondly, Sm^{3+} doping regulates the carrier concentration in the doped fibers, and the propagation of light in semiconductors is closely related to the plasma wavelength. Sm^{3+} doping increases the carrier concentration, provides a new donor energy level (Sm^{3+}), and enhances the plasma effect[7,37]. Meanwhile, the increase in carrier concentration leads to $\lambda < \lambda_p$. Thus, the doped fibers have dielectric characteristics, namely the low reflectivity[35]. Thirdly, the electrons in Sm^{3+} are excited to transit from $^6H_{5/2}$ to $^6H_{9/2}$[17], and then an absorption band appears at wavelength of 1000 – 1100 nm, thus resulting in the low reflectivity at wavelength of 1.06 μm, as shown in Fig.8b.

2.7 Resistivity and infrared emissivity

The working band of infrared detectors is generally 3–5 and 8–14 μm. The infrared emissivity of $Sn_{1-x}Sm_xO_2$ micro/nano-fibers with x=0wt%, 8wt%, 16wt%, and 24wt% at wavelength of 3–5 μm is 0.742, 0.685, 0.596, and 0.638, respectively, as listed in Table 1. The working band of thermal imaging system is usually 8–14 μm. Fig.9 presents the resistivity and infrared emissivity at wavelength of 8–14 μm of $Sn_{1-x}Sm_xO_2$ micro/nano-fibers. It can be seen that the infrared emissivity and resistivity have similar change trends: with increasing the Sm doping amount, the infrared emissivity is decreased firstly and then increased. When x=16wt% , the lowest infrared emissivity is achieved as 0.749.

Table 1 Infrared emissivity of $Sn_{1-x}Sm_xO_2$ micro/nano-fibers at wavelength of 3–5 μm

x	0wt%	8wt%	16wt%	24wt%
Infrared emissivity	0.742	0.685	0.596	0.638

According to Kirchhoff's law[38], the infrared emissivity is related to reflectivity, as follows:

$$\varepsilon_\lambda = 1 - R_\lambda \quad (2)$$

where λ is the wavelength, R_λ is the reflectivity at wavelength of λ, and ε_λ is the infrared emissivity at wavelength of λ.

In the infrared spectrum, reflectivity is related to the electrical performance and it is mainly reflected by the complex refractive index and complex dielectric constant, based on the free electron theory[39], as follows:

$$R = \frac{(n - n_0)^2 + k^2}{(n + n_0)^2 + k^2} \quad (3)$$

$$\varepsilon'' = 2nk \approx \frac{1}{2\pi\varepsilon_0\rho f} \quad (4)$$

where R is the reflectivity, n is refractive index, k is extinction coefficient, n_0 is vacuum refractive index, ε'' is the imaginary part of dielectric constant, ε_0 is vacuum dielectric constant, ρ is resistivity, and f is electromagnetic frequency. In the middle and far infrared band (λ >5 μm), the relationship between infrared emissivity and resistivity can be obtained, according to the Hagen-Rubens approximate equation[40], as follows:

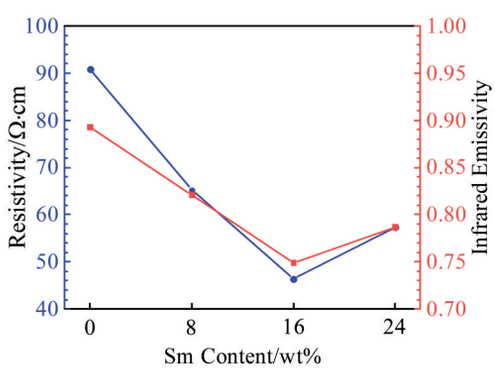

Fig.9 Resistivity and infrared emissivity of $Sn_{1-x}Sm_xO_2$ micro/nano-fibers

$$E_\omega \approx 2\sqrt{2\varepsilon_0\omega\rho} \quad (5)$$

where E is the infrared emissivity and ω is the incident frequency of electromagnetic wave. According to Eq. (5), when the incident frequency of electromagnetic wave is constant, the infrared emissivity is positively correlated with the resistivity, i. e., the higher the resistivity, the higher the infrared emissivity. On the one hand, SnO_2 is a typical oxide semiconductor material, and its main form of carrier is free electrons in the lattice. The Sm^{3+} enters the SnO_2 lattice and causes ion replacement because of the difference in valance and ion radius of Sn^{4+} and Sm^{3+}. As a result, a large number of oxygen vacancy defects and the novel donor energy levels (Sm^{3+}) are generated, which increases the number of free electrons, improves the carrier concentration of the doping system, and reduces the resistivity[41]. However, with further increasing the Sm doping amount from 16wt% to 24wt%, the resistivity is increased slightly. This is because the excessive doping may cause lattice distortion of SnO_2, which results in interface enlargement and the reduction of electron migration[42]. On the other hand, the micro/nano-fibers have special 3D network morphology, which can provide a convenient transmission path for carrier transmission[36], thus facilitating the formation of 3D conductive network. Moreover, the 3D network morphology of micro/nano-fibers has a large specific surface area, which can further improve the conductivity of ions[22,36–37] and enhance the electrical performance of the doping fibers.

The $Sn_{0.84}Sm_{0.16}O_2$ micro/nano-fibers and epoxy resin were mixed evenly at volume ratio of 1∶1 and then coated on the high-emissivity ceramic sheets (infrared emissivity of 0.749, right wafer in Fig. 10). The uncoated customized high-emissivity ceramic sheets (infrared emissivity of 0.913, left wafer in Fig. 10) was used as control group for the infrared thermography comparison. These round ceramic sheets were placed on the heating device at 40 °C, as shown in Fig. 10a. Fig. 10b – 10e show the infrared thermography images of $Sn_{0.84}Sm_{0.16}O_2$ micro/nano-fiber coating heated at 40 °C for 0, 1, 2, and 3 min, respectively. Because the infrared thermography barely changes after heating for 3 min, the heating duration was set as 3 min. It can be seen that with the heating proceeding, the infrared radiation of both the wafers is gradually increased. However, the infrared radiation of the right wafer is significantly lower than that of the left wafer, indicating that the $Sn_{0.84}Sm_{0.16}O_2$ micro/nano-fibers have low infrared emissivity and can effectively reduce the infrared radiation on the material surface. It can be inferred that the $Sn_{0.84}Sm_{0.16}O_2$ micro/nano-fibers have great potential as the infrared stealth material.

2.8 First-principles analysis

The first-principles calculations were performed for the $Sn_{1-x}Sm_xO_2$ micro/nano-fibers. The supercell structure model of 1×2×3 was constructed, containing 24 O atoms and 12 Sn atoms. In order to reduce the edge effect, Sm atoms were used to replace the Sn atoms in the middle. The doping model is shown in Fig. 11a and 11b, and the doping amount is 16wt%. The band structures of SnO_2 and $Sn_{0.84}Sm_{0.16}O_2$ micro/nano-fibers are shown in Fig. 11c and 11d, respectively. The bottom of the conduction band and the top of the valence band of the specimens are located at G point in the Brillouin region, indicating that SnO_2 before and after doping is still a semiconductor with direct bandgap. Compared with those of SnO_2, the conduction band and valence band curves of the $Sn_{0.84}Sm_{0.16}O_2$ micro/nano-fibers become denser and smoother, and new conduction band and valence band appear. The bottom and top of the conduction band move closer to the Fermi level, enhancing the coating conductivity. This is mainly due to the effect of 4f orbit of Sm atom, which results in the appearance of the impurity level at the bottom of conduction band. The valence band carriers can be directly transformed to the impurity level and then to the conduction band, which reduces the energy loss and strengthens the electrical performance of the doped fibers, leading to a smaller band gap width[43]. The state density distributions of SnO_2 and $Sn_{0.84}Sm_{0.16}O_2$ micro/nano-fibers are shown in Fig. 11e and 1f, respectively. The conduction band energy of the doped fibers is mainly contributed by the Sn 5s and Sn 5p, and that of the upper valence band is mainly contributed by Sn 5s, Sn 5p, and O 2p. The lower valence band energy is mainly contributed by Sn 5s, Sn 5p, and O 2s. In addition, the Sm 4f contributes to the energy of lower conduction band and upper valence band of the doped fibers. The Sm 4f concentrated at the bottom of conduction band and the top of valence band forms a large number of impurity energy levels, provides a large number of hole carriers for the doped fibers, promotes the electron

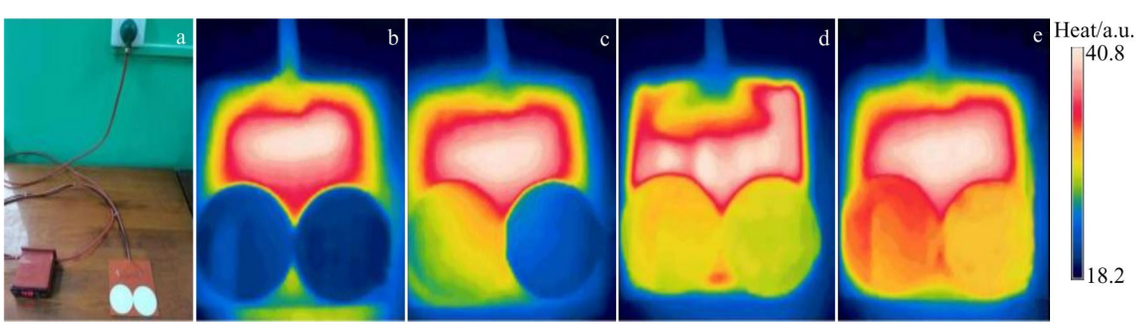

Fig.10 Appearance of heating device for infrared thermography comparison (a); infrared thermography images of coated and uncoated ceramic sheets heated at 40 °C for 0 min (b), 1 min (c), 2 min (d), and 3 min (e)

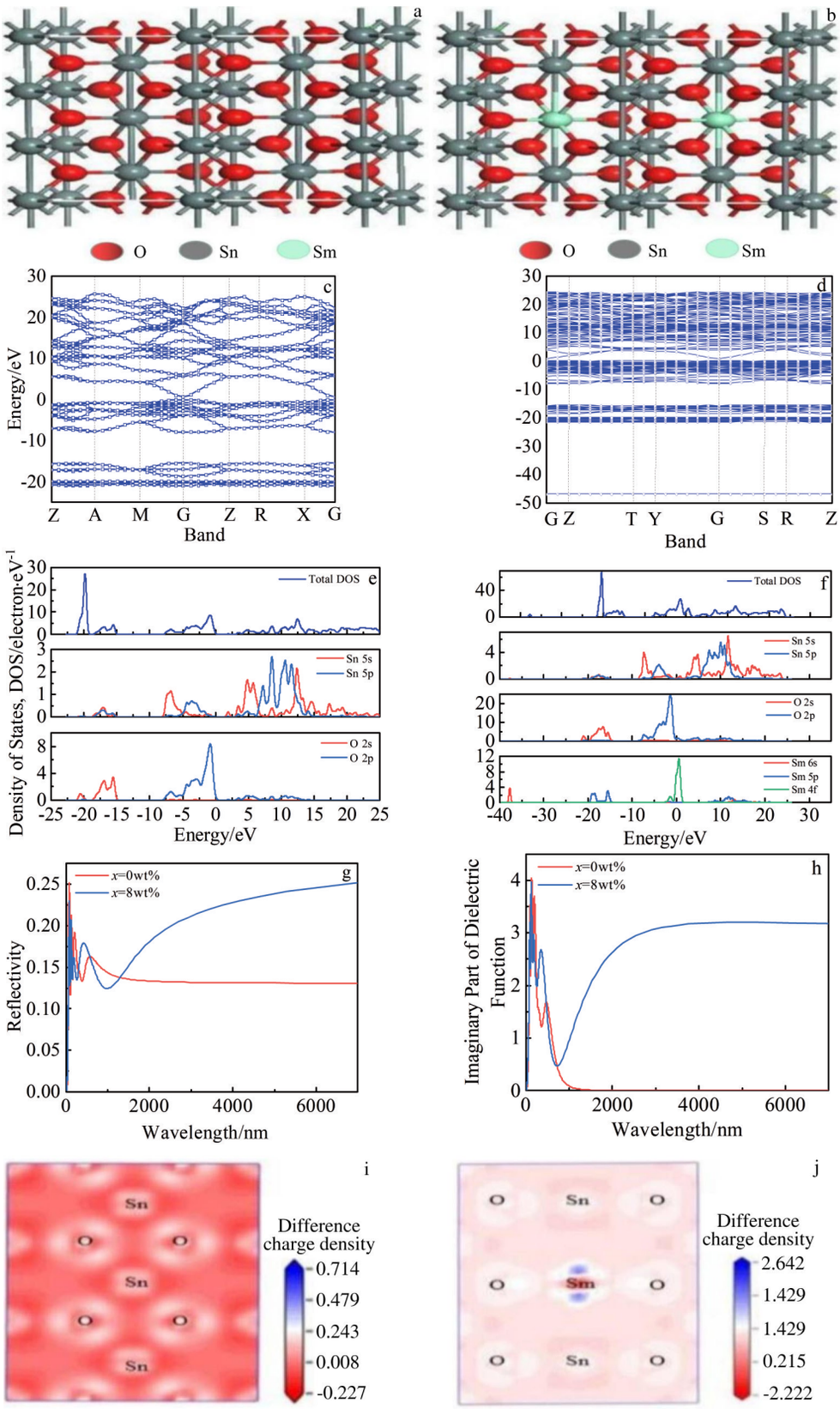

Fig.11 Lattice models (a, b), band structures (c, d), density of states (e, f), reflectivity (g), imaginary part of dielectric function (h), and difference charge densities (i, j) of SnO_2 (a, c, e, i) and $Sn_{0.84}Sm_{0.16}O_2$ micro/nano-fibers (b, d, f, j)

transfer, increases the degree of electron sharing, enhances the localization, and strengthens the plasma effect. Besides, the laser reflectivity reduces, the conductivity improves, and the infrared emissivity reduces. The reflectivity of SnO_2 and $Sn_{0.84}Sm_{0.16}O_2$ micro/nano-fibers is shown in Fig. 11g. Compared with SnO_2, the $Sn_{0.84}Sm_{0.16}O_2$ micro/nano-fibers

have an obvious reflection valley (absorption peak) at wavelength of 1.06 μm, and have a higher infrared absorption rate. It can also be seen that the $Sn_{0.84}Sm_{0.16}O_2$ micro/nano-fibers have a high infrared reflectivity in the infrared band, which leads to the low infrared emissivity. The imaginary part of the dielectric function of the SnO_2 and $Sn_{0.84}Sm_{0.16}O_2$ micro/nano-fibers is shown in Fig. 11h, which represents the dipole formation energy and directly reflects the actual transition of electrons between the filled and unfilled states. The higher the value of imaginary part, the higher the probability of transition generation[44–45]. It can be seen from Fig. 11h that the $Sn_{0.84}Sm_{0.16}O_2$ micro/nano-fibers have a larger imaginary part of dielectric function at wavelength of 1.06 μm than the SnO_2 does, which is prone to electron transition at wavelength of 1.06 μm, thus resulting in the laser absorption. The electron density of SnO_2 and $Sn_{0.84}Sm_{0.16}O_2$ micro/nano-fibers is shown in Fig. 11i and 11j, respectively. It can be seen from Fig. 11i that in SnO_2, the Sn atom is light white, while the O atom is light red, indicating that the Sn atom gains a small number of electrons and the O atom loses a small number of electrons. According to Fig. 11j, in the $Sn_{0.84}Sm_{0.16}O_2$ micro/nano-fibers, the center of the Sm atom is red, indicating that its electron loss is severe. The surrounding area of Sm atom is blue, which indicates that a positive charge is around the Sm atom. By comparing the values of chromaticity markers and chromatic aberration, it can be seen that Sm^{3+} is the main reason for the increased carrier concentration. The carrier concentration affects the wavelength of plasma, which results in low reflectivity at wavelength of 500–1500 nm and low emissivity in the infrared bands. The simulation results are consistent with the experiment analyses, and the effect mechanism of Sm^{3+} doping on the infrared emissivity and laser absorption of SnO_2 from the perspective of electronic structure was discussed.

3 Conclusions

1) In $Sn_{1-x}Sm_xO_2$ (x=0wt%, 8wt%, 16wt%, 24wt%) micro/nano-fibers prepared by electrospinning combined with heat treatment, Sm^{3+} enters the SnO_2 lattice by replacing Sn^{4+}, and the morphology presents staggered irregular network fiber structures. The fibers are continuous and the elements are evenly distributed on the fiber.

2) When x=16wt% , the optimal laser reflectivity and infrared emissivity can be achieved for $Sn_{1-x}Sm_xO_2$ micro/nano-fibers. The infrared emissivity is 0.749 at wavelength of 8–14 μm, the reflectivity is 53.9% at wavelength of 1064 nm, and the reflectivity is 38.5% at wavelength of 1550 nm, showing great potential as the laser-infrared compatible stealth material.

3) The three-dimensional network of micro/nano-fibers has a large specific surface area, which improves the charge transfer efficiency and conductivity, thereby ensuring the high light absorption performance and low infrared emissivity. Sm^{3+} doping improves the carrier concentration in the fibers, introduces a new impurity level, reduces the band gap width, and enhances the plasma effect and electrical performance, thus improving the infrared and laser compatible stealth performance. Moreover, Sm^{3+} doping increases the probability of electron transition in the fibers. The excited electron transition from $^6H_{5/2}$ to $^6H_{9/2}$ in Sm^{3+} results in the absorption band at 1000 – 1100 nm, which enhances the absorption performance at wavelength of 1.06 μm.

References

1 Feng Lili, Liu Yiman, Yao Lin *et al. Progress in Chemistry*[J], 2021, 33(6): 1044 (in Chinese)

2 Chen X L, Tian C H, Che Z X *et al. Optik*[J], 2018, 172: 840

3 Zhao X K, Zhao Q W, Wang L F. *Procedia Engineering*[J], 2011, 15: 1668

4 Miao L, Shi J M, Wang J C *et al. Optical Engineering*[J], 2016, 55(5): 57 101

5 Kim J, Han K, Hahn J W. *Scientific Reports*[J], 2017, 7(1): 6740

6 Zhang C L, Huang C, Pu M B *et al. Scientific Reports*[J], 2017, 7(1): 5652

7 Qin Y S, Zhang M J, Guan Y *et al*. *Ceramics International*[J], 2019, 45(11): 14 312

8 Xia Yuanjia, Zhao Fang, Li Zhizun *et al. New Chemical Materials*[J], 2022, 50(5): 38 (in Chinese)

9 Wu Lingzhi, Xie Guohua, Wu Ruibin *et al. Aerospace Materials & Technology*[J], 2001, 31(2): 1 (in Chinese)

10 Wang Q, Zhu J Y, Wang H H *et al. Materials Today: Energy*[J], 2019, 11: 199

11 Lin Wenxue, Liu Jinsong. *Science Information*[J], 2007(11): 50 (in Chinese)

12 Zhang H Y, Yu M, Du Y *et al. Materials Chemistry and Physics*[J], 2022, 285: 126 069

13 Liang Jingnan, Fu Cunlin, Cai Wei *et al. Rare Metal Materials and Engineering*[J], 2012, 41(S2): 197 (in Chinese)

14 Yu Feng, Wang Peiji, Zhang Changwen. *Acta Physica Sinica*[J], 2010, 59(10): 7285 (in Chinese)

15 Su X L, Jia Y, Wang J B *et al. Arabian Journal for Science and Engineering*[J], 2015, 40(10): 2969

16 Lu Yanli, Zhang Shuanqin, Jiang Xiaojun *et al. Acta Armamentarii*[J], 2011, 32(12): 1514 (in Chinese)

17 Zhu Y Q, Han P D, Zhang L *et al. Journal of Rare Earths*[J], 2013, 31(11): 1102

18 Han P D, Huang X G, Zhang Q T. *Rare Metals*[J], 2011, 30(6): 616

19 He W, Zhang J, Wang L X *et al. Journal of Rare Earths*[J], 2009, 27(2): 231

20 Zhang D W, Xu X, Diao J L *et al. Integrated Ferroelectrics*[J], 2020, 210(1): 167

21 Li Leiwei, Lv Yong, Niu Chunhui. *Laser & Infrared*[J], 2018, 48(1): 83 (in Chinese)

22 Ramakrishna S, Fujihara K, Teo W E *et al. Materials Today*[J], 2006, 9(3): 40

23 Zhao R, Lu X F, Wang C. *Composites Communications*[J], 2018,

10: 140
24 Wang Xinkun, Zhao Fang, Wang Jianjiang. *Materials Reports*[J], 2019, 33(S2): 83 (in Chinese)
25 Liu Jiawei, Wang Jianjiang, Xu Baocai *et al. Journal of Aeronautical Materials*[J], 2017, 37(5): 29 (in Chinese)
26 Li Junshou, Shi Suilin, Zhao Fang *et al. Rare Metal Materials and Engineering*[J], 2013, 42(S1): 6 (in Chinese)
27 Yan Jun, Cui Haiping, You Yucong *et al. Rare Metal Materials and Engineering*[J], 2007, 36(S1): 873 (in Chinese)
28 Wagner R S, Ellis W C. *Applied Physics Letters*[J], 1964, 4(5): 89
29 Wu Y, Yang P. *Journal of the American Chemical Society*[J], 2001, 123(13): 3165
30 Yang P, Lieber C M. *Science*[J], 1996, 273(5283): 1836
31 Zhang L, Ren X, Luo Y L *et al. Chemical Communications*[J], 2018, 54(92): 12 966
32 Lei J L, Hu L, Zhang J *et al. Applied Surface Science*[J], 2020, 499: 143 931
33 Dasireddy V D B C, Logar N Z, Kovač J *et al. Catalysis Science & Technology*[J], 2022, 12(9): 2990
34 Zhang Yulong, Li Ping, Shi Lei. *Stealth Materials*[M]. Beijing: Chemical Industry Press, 2018: 203 (in Chinese)
35 Mao Yuhui, Zhang Shengli, Luo Wenhai *et al. Glass*[J], 2012, 39(4): 44 (in Chinese)
36 Kumar P S, Sundaramurthy J, Sundarrajan S *et al. Energy & Environmental Science*[J], 2014, 7(10): 3192
37 Kim H, Pique A. *Applied Physics Letters*[J], 2004, 84(2): 218
38 Oguchi H, Heilweil E J, Josell D *et al. Journal of Alloys and Compounds*[J], 2009, 477(1–2): 8
39 Mott N F, Jones H. *The Theory of the Properties of Metals and Alloys*[M]. Oxford: Clarendon Press, 1936
40 Sokolov A V. *Optical Properties of Metals*[M]. New York: Elsevier, 1967
41 Mei Songbai, Ning Wei, Wang Qingwei *et al. Journal of Synthetic Crystals*[J], 2009, 38(4): 943 (in Chinese)
42 Tyuliev G, Angelov S. *Applied Surface Science*[J], 1988, 32(4): 381
43 Sun Shaoqi, Wang Jingqin, Zhu Yancai *et al. Materials Reports* [J], 2020, 34(Z1): 48 (in Chinese)
44 Zhang Lili, Xia Tong, Liu Guian *et al. Acta Physica Sinica*[J], 2019, 68(1): 245 (in Chinese)
45 Xu Benchao, Wang Xin, Wen Jing *et al. Journal of Wuhan University of Technology*[J], 2010, 32(22): 172 (in Chinese)

$Sn_{1-x}Sm_xO_2$微纳米纤维的红外发射率与激光吸收性能：实验研究与第一性原理仿真

夏元佳[1]，赵　芳[1]，李志尊[1]，程兆刚[1]，许宝才[2]
(1. 陆军工程大学石家庄校区，河北 石家庄 050003)
(2. 河北工业职业技术大学，河北 石家庄 050091)

摘　要：采用静电纺丝法结合热处理工艺制备了$Sn_{1-x}Sm_xO_2$（x=0%，8%，16%，24%，质量分数，下同）微纳米纤维，表征了产物的物相、形貌、激光吸收性能和红外发射率，同时基于密度泛函理论的第一性原理对比分析了$Sn_{1-x}Sm_xO_2$（x=0%， 16%）的相关光电性质，进一步从电子结构角度解释了Sm^{3+}掺杂对SnO_2红外发射率和激光吸收的作用机理。结果表明：经600 ℃煅烧后，$Sn_{1-x}Sm_xO_2$均为单一金红石型结构，呈现出良好的纤维形貌，纤维相互交错，形成无规则三维网状结构，且各元素在纤维上分布均匀。随着Sm^{3+}掺杂量的增大，产物在1064和1550 nm处的反射率逐渐降低，红外发射率先减小后增大。当x=16%时，在1064 nm处的反射率为53.9%，在1550 nm处的反射率为38.5%，在8–14 μm波段的红外发射率为0.749，为“薄轻宽强”的新型激光与红外兼容隐身材料提供了一定的理论与实践依据。

关键词：微纳米纤维；激光吸收；红外发射率；第一性原理；半导体

作者简介：夏元佳，男，1998年生，硕士生，陆军工程大学石家庄校区，河北 石家庄 050003，E-mail：1220563265@qq.com